

Neural Field-Based 3D Surface Reconstruction of Microstructures from Multi-Detector Signals in Scanning Electron Microscopy

Shuo Chen¹ Yijin Li² Xi Zheng³ Guofeng Zhang^{1*}

¹State Key Lab of CAD&CG, Zhejiang University, Hangzhou 310058, China

²Alibaba Group, Hangzhou 311121, China

³Analysis Center of Agriculture, Life and Environment Sciences, Zhejiang University, Hangzhou 310058, China
chenshuo.eric@zju.edu.cn, liyijin.lyj@alibaba-inc.com, xzheng@zju.edu.cn, zhangguofeng@zju.edu.cn

Abstract

The scanning electron microscope (SEM) is a widely used imaging device in scientific research and industrial applications. Conventional two-dimensional (2D) SEM images do not directly reveal the three-dimensional (3D) topography of micro samples, motivating the development of SEM 3D surface reconstruction methods. However, reconstruction of complex microstructures remains challenging for existing methods due to the limitations of discrete 3D representations, the need for calibration with reference samples, and shadow-induced gradient errors. Here, we introduce NFH-SEM, a neural field-based hybrid SEM 3D reconstruction method that takes multi-view, multi-detector 2D SEM images as input and fuses geometric and photometric information into a continuous neural field representation. NFH-SEM eliminates the manual calibration procedures through end-to-end self-calibration and automatically disentangles shadows from SEM images during training, enabling accurate reconstruction of intricate microstructures. We validate the effectiveness of NFH-SEM on real and simulated datasets. Our experiments show high-fidelity reconstructions of diverse, challenging samples, including two-photon lithography microstructures, peach pollen, and silicon carbide particle surfaces, demonstrating precise detail and broad applicability.

Introduction

The scanning electron microscope (SEM) ¹ is a powerful imaging tool that uses a focused electron beam to scan a sample surface, generating signals such as secondary electrons (SE) and backscattered electrons (BSE) to produce high-resolution, micro- to nanoscale images. Owing to its remarkable depth of field, spatial resolution, and stereoscopic appearance, SEM has been widely adopted in fields

such as materials science ², biomedicine ³, and semiconductor manufacturing ⁴. However, SEM images inherently represent two-dimensional (2D) intensity distributions of scattered electrons captured by detectors, which do not directly convey the underlying three-dimensional (3D) surface geometry. This limitation poses a significant barrier in applications that require accurate 3D characterization, such as analysis of biological surface structures ⁵ or advancing the precision of manufacturing ⁶. As a result, reconstructing detailed 3D surface topography from 2D SEM images has emerged as a critical requirement of growing importance. Existing approaches for SEM 3D surface reconstruction primarily fall into three categories ⁷: multi-view, single-view, and hybrid methods.

Multi-view methods ⁷⁻¹¹ are typically based on the structure-from-motion (SfM) technique ¹²⁻¹⁴, which estimates 3D surface geometry from a sequence of tilted-view SEM images. These methods triangulate matched features between views to recover a sparse 3D point cloud, followed by dense reconstruction to generate a more complete 3D model. However, reliable feature matching becomes challenging in smooth and textureless regions, which are particularly prevalent in microscale sample surfaces. Therefore, such regions often suffer from poor reconstruction quality.

Single-view methods ¹⁵⁻²¹, mainly based on the photometric stereo (PS) technique ²²⁻²⁴, reconstruct 3D models from images captured under varying illumination of a fixed viewpoint. In SEM, this is achieved using a four-quadrant backscattered electron (4Q-BSE) detector, a ring detector segmented into four quadrants placed beneath the objective lens (Fig. 1a), which independently captures BSE signals from four directions. By leveraging the nearly Lambertian distribution of BSE signals ¹, surface gradients can be estimated and integrated into height maps. However, single-view methods suffer from the following challenges. First, gradient integration can only recover continuous surface variations and fails to capture discontinuities

*Corresponding author

or steep topographies. Second, accurate reconstruction requires a complex calibration process relying on reference samples with known geometry to determine detector parameters^{15,16,19}. Third, one major drawback of single-view methods is their inability to handle shadows in BSE images. Shadows caused by geometric occlusion (Fig. 1b) violate the theoretical model of PS¹⁵, leading to erroneous gradient estimation and distorted 3D models. These limitations constrain single-view methods to smooth surfaces with minimal shadowing effects.

Hybrid methods^{25,26} aim to combine the complementary strengths of multi-view and single-view methods, making use of the former’s applicability for textured surfaces and the latter’s effectiveness on smooth regions. Typically, hybrid methods first use multi-view methods to recover a coarse global geometry and then use single-view methods to refine surface details. Despite their potential, existing hybrid methods remain constrained by some significant issues. First, current works^{25,26} rely on 2D height maps to fuse the geometric information from these two methods. However, this representation is inherently inadequate for capturing complex 3D structures. Second, a parameter calibration procedure is generally required in the single-view step. Third, the shadowing remains unresolved, still resulting in reconstruction errors. Consequently, current hybrid methods exhibit limited suitability, particularly for complex samples with significant shadowing effects.

In this work, we propose a neural field-based hybrid SEM 3D reconstruction framework, NFH-SEM, which reconstructs high-fidelity 3D surface models of microstructures using SEM images acquired from multiple viewpoints and detectors. Neural fields²⁷ are a class of techniques that represent the geometry and physical properties of 3D space using coordinate-based neural networks. They have recently achieved remarkable success in 3D reconstruction^{28–30} and rendering^{31–33} tasks in computer vision. Beyond conventional RGB imaging, neural field representations have been successfully extended to various data modalities^{34–36}. Recent studies^{37–40} further indicate their applicability to microscopy imaging systems, significantly enhancing the 3D characterization of micro- and nanoscale samples. These advances motivate us to explore neural fields as a promising representation for SEM 3D surface reconstruction. In addition, the proposed novel framework also eliminates the need for parameter calibration and effectively deals with SEM shadowing effects. Overall, NFH-SEM includes the following key features:

- NFH-SEM enhances the reconstruction of complex microstructures by integrating geometric constraints from SfM and surface gradient cues from PS into a unified neural field through carefully designed training supervision. Unlike height map representation in previous methods, the neural field provides a continuous and expressive rep-

resentation of complex 3D surfaces. These designs improve both global geometry and local surface detail.

- NFH-SEM eliminates the need for parameter calibration with reference samples. We construct the mapping between sample geometry and the intensity distributions in 4Q-BSE images as a learnable forward model. The model parameters are optimized end-to-end along with the neural field, enabling self-calibration reconstruction.
- NFH-SEM is highly robust to SEM shadows. We introduce an iterative shadow separation strategy that automatically detects and excludes shadowed regions during training, enabling the network to focus on reliable photometric cues. In our experiments, NFH-SEM can directly take BSE images with pronounced shadowing as input. Compared to the distorted gradient produced by PS methods, NFH-SEM is able to extract accurate surface information. This overcomes the limitation that previous methods can only be applied to shadow-free samples.

We validate NFH-SEM on various samples with different geometry features, including two-photon lithography (TPL)-printed microstructures, peach pollen, and silicon carbide (SiC) particle surfaces. The experimental results demonstrate that our method achieves accurate, detail-rich 3D reconstructions across diverse settings, showing strong generalization and practical applicability.

Results

Reconstruction Pipeline of NFH-SEM

NFH-SEM is a neural field-based hybrid method for SEM 3D reconstruction, designed to recover the surface geometry of complex microstructures from 2D SEM images. As shown in Fig. 1, the reconstruction pipeline consists of three steps: multi-view and multi-detector SEM data acquisition, SfM-based geometric initialization, and a three-stage neural field hybrid training process.

During data acquisition (Fig. 1a), the sample is mounted on a motorized stage inside the SEM chamber, which is systematically tilted and rotated to capture a comprehensive set of views. At each viewpoint, an in-chamber SE detector and a 4Q-BSE detector, standard configurations in modern SEM systems, simultaneously acquire one SE image and four BSE images. As illustrated in Fig. 1b, each BSE quadrant captures electrons from a specific direction, forming an image that resembles illumination from that direction. Moreover, due to the geometric self-occlusion of the sample, BSE signals may be blocked from reaching certain quadrants, resulting in dark regions in the corresponding BSE images, known as the SEM shading effect. These shadows are unrelated to local surface gradients and thus violate the assumptions of previous PS methods^{15,19}, leading to inaccurate gradient estimation in such areas.

Next, we apply the SfM method to initialize the hybrid reconstruction process (Fig. 1c). Following previous stud-

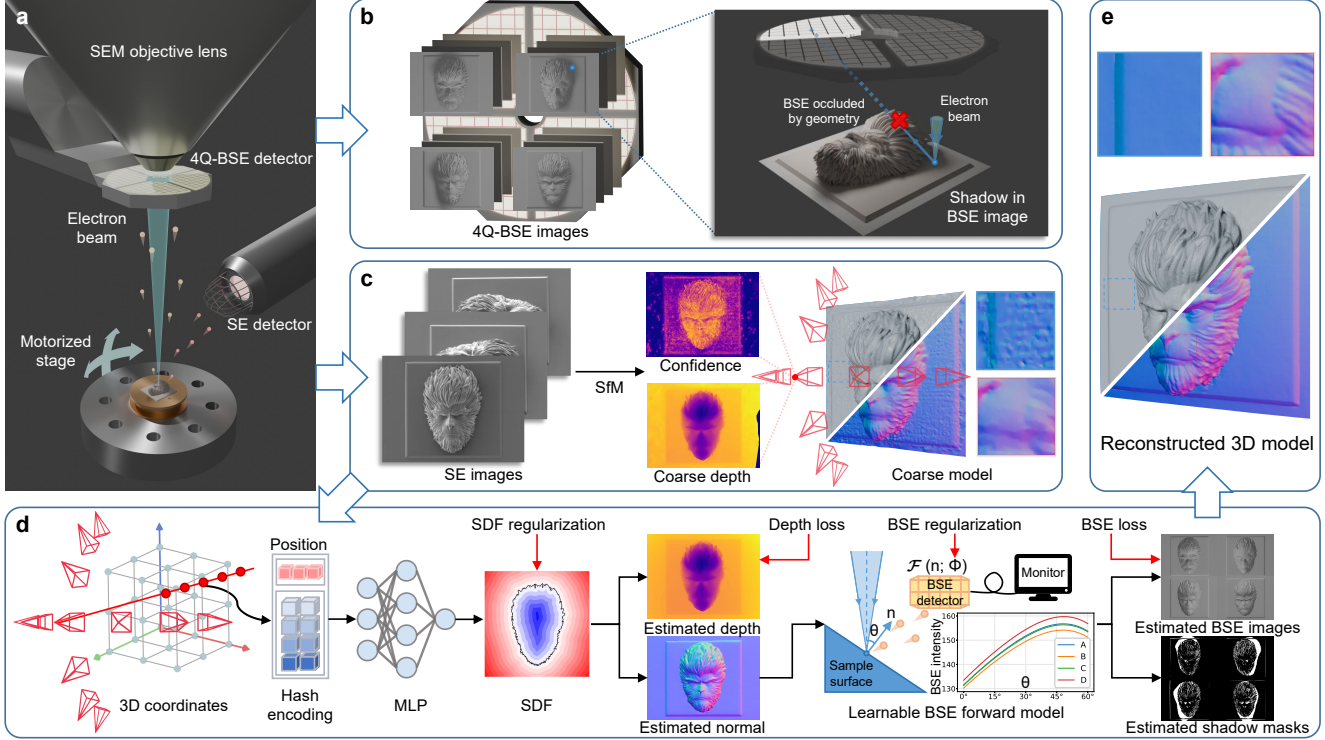


Fig. 1 | Workflow of NFH-SEM. **a**, The sample is mounted on a motorized stage for controlled tilting and rotation. At each viewpoint, SEM images are simultaneously captured from the 4Q-BSE and SE detectors. **b**, Each BSE image presents different directional illumination, and contains considerable shadows caused by geometric occlusion of BSE signals. **c**, Multi-view SE images are first processed via SfM to obtain a coarse 3D model, along with per-view depth and confidence maps. **d**, The posed depth maps and 4Q-BSE images jointly supervise the training of a neural field, which is implemented as an MLP that maps hash-encoded 3D coordinates to SDF values. Concurrently, a learnable BSE forward model is self-calibrated to map geometry to 4Q-BSE image intensities while disentangling shadows. **e**, The reconstructed model is finally extracted from the neural field, exhibiting notable improvements in accuracy and surface detail.

ies⁹⁻¹¹, we use multi-view SE images for SfM reconstruction. Despite the fundamental differences between SEM and conventional optical imaging, prior studies have shown that the traditional photogrammetry SfM method can also be applied to multi-view SEM data by treating each SEM image as captured by a virtual camera. However, SfM is limited in textureless regions where reliable feature matching cannot be established. As a result, this step can only provide a coarse estimate of the sample geometry. We extract per-view depth maps z and associated confidence maps w from the SfM output, which serve as geometric priors in the subsequent neural field training.

In NFH-SEM (Fig. 1d), the 3D geometry is implicitly modeled as a signed distance function (SDF)⁴¹, parameterized by a multilayer perceptron (MLP)²⁸, denoted as \mathcal{M} with learnable parameters Θ . During forward inference, each pixel in SEM images is projected to a viewing ray with a sequence of sample points. The 3D coordinate x of each point is encoded using multi-resolution hash encoding⁴² to generate feature vectors, which are then passed to the MLP to predict the corresponding SDF value $s = \mathcal{M}(x; \Theta)$. To effectively integrate hybrid cues from both SfM and PS

into the neural field while maintaining training stability, we adopt a three-stage training strategy.

In the first stage, the neural field is initialized using only SfM geometric supervision to establish coarse global geometry and mitigate convergence to poor local minima. Supervision is applied via a depth loss $\mathcal{L}_{\text{depth}}$ between the SfM depth z and the predicted depth \hat{z} , extracted from the SDF. Per-pixel confidence weights w are applied to modulate the loss function, guiding the network to focus on more reliable SfM reconstructed regions during training.

The second stage further fuses photometric cues derived from 4Q-BSE images to refine surface geometry. Prior PS-based methods^{15,16,19} rely on empirical models to relate local surface normals to BSE signal intensities, and directly compute surface gradients from 4Q-BSE images. However, in practice, such models require a complex calibration process for detector parameters and often exhibit discrepancies from the real BSE signal distribution, especially in shadowed regions, thereby limiting the reliability of gradient estimation. On the contrary, we avoid explicit gradient computation and implicitly transport surface gradient information encoded in BSE images to the neural field. Specifically,

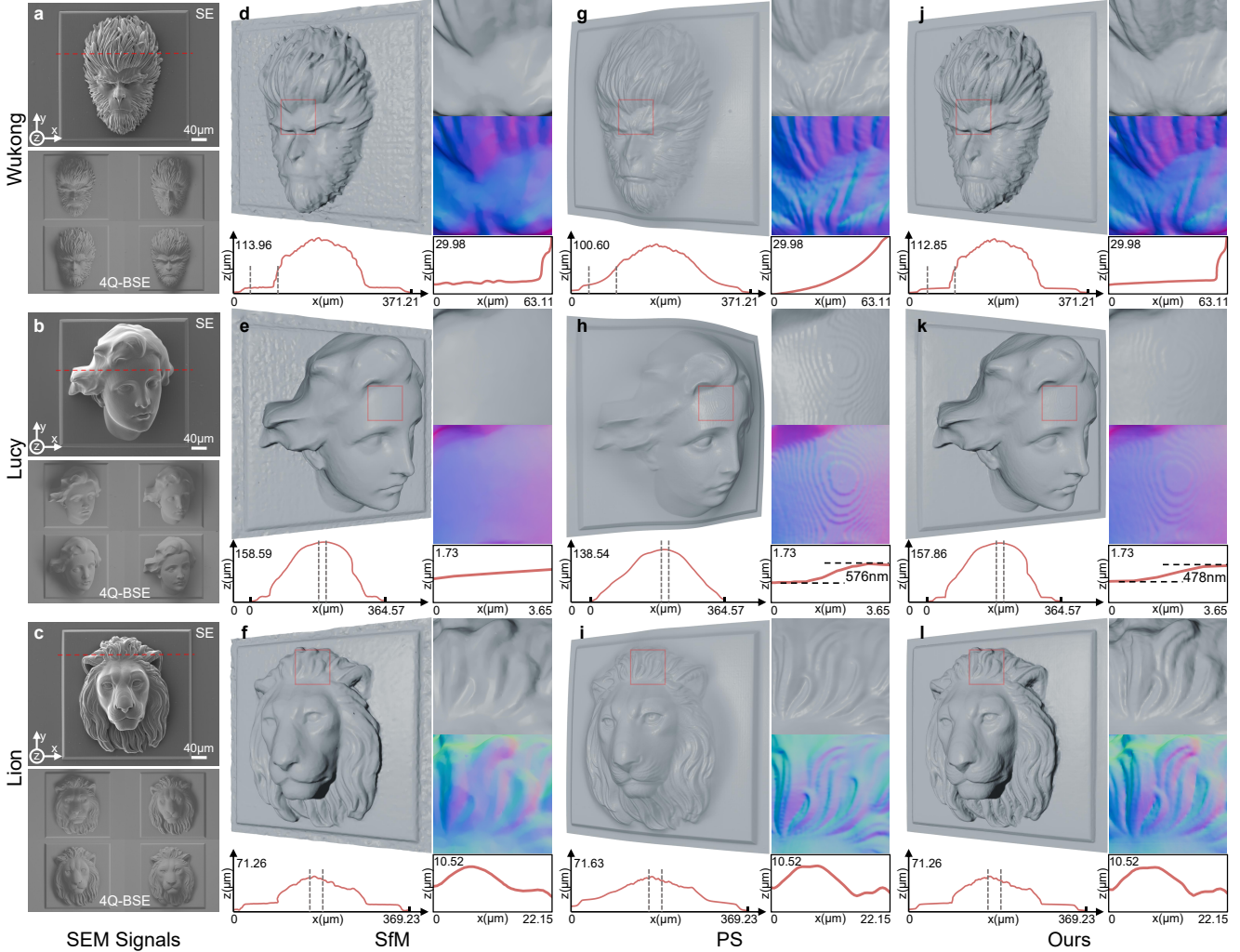


Fig. 2 | Reconstruction comparison on microstructures fabricated by two-photon lithography. **a–c**, Top-view SE and 4Q-BSE images of the fabricated microstructures. **d–f**, Reconstructions using the SfM method. **g–i**, Reconstructions using the PS method. **j–l**, Reconstructions using the proposed NFH-SEM. Red boxes in **d–l** indicate regions enlarged together with normal maps to highlight the reconstruction detail and accuracy of NFH-SEM. Cross-sectional profiles in **d–l** correspond to the red lines in **a–c**, with zoomed-in regions marked between vertical grey lines. Layer heights are annotated in **h** and **k**. Additional visualizations are provided in Supplementary Video 1.

we model the mapping from surface normal, $\hat{n} = \nabla s$, to BSE intensity as a learnable forward model \mathcal{F} with parameters $\hat{\Phi}$. A photometric loss \mathcal{L}_{BSE} is then defined between the synthesized BSE images $\mathcal{F}(\hat{n}; \hat{\Phi})$ and the captured BSE images b , enabling joint optimization of both the neural field $\hat{\Theta}$ and the forward model $\hat{\Phi}$ via backpropagation. This approach allows \mathcal{F} to fit the distribution of real BSE signals adaptively and eliminates the need for manual calibration, effectively embedding surface gradient information into the neural field representation.

In the final stage, we introduce an iterative masking scheme that excludes shadowed regions of BSE images from supervision, further improving reconstruction accuracy. We observe that areas with high BSE loss often correspond to shadows, because image intensity in these ar-

reas is not relative to the local geometry, and thus cannot be modeled by \mathcal{F} . Based on this observation, we iteratively refine binary shadow masks to separate valid supervision regions from shadowed areas. This establishes a self-reinforcing feedback loop. The shadow masks lead to higher-quality supervision, enabling more accurate geometry and forward model \mathcal{F} , which in turn refine the masks and gradually mitigate shadow interference. Ultimately, this process produces shadow-free synthesized 4Q-BSE images and per-view shadow masks S , enabling reliable surface reconstruction even in the presence of significant shadowing.

Each training stage of the neural field starts from the parameters $\hat{\Theta}$ and $\hat{\Phi}$ of the previous stage, progressively incorporating additional loss terms. The complete training

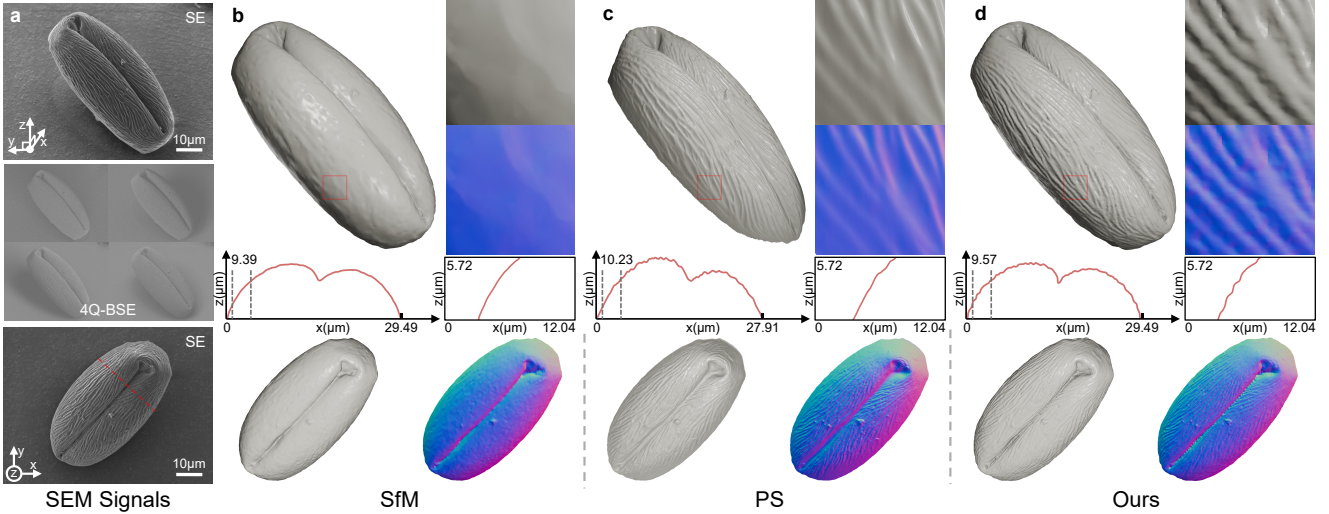


Fig. 3 | Reconstruction comparison on peach pollen. **a**, Side-view SE and 4Q-BSE images, and a top-view SE image of the pollen grain. **b**, Reconstruction using the SfM method. **c**, Reconstruction using the PS method. **d**, Reconstruction using the proposed NFH-SEM. In **b–d**, differences in sidewall textures are highlighted with red boxes and cross-sectional views. The bottom row shows top views of the reconstructed models along with their surface normals. Additional visualizations are provided in Supplementary Video 2.

objective can be summarized as minimizing \mathcal{L} :

$$\mathcal{L} = \mathcal{L}_{\text{depth}}(\hat{z}, z) + \mathcal{R}_s + \mathcal{L}_{\text{BSE}}(\mathcal{F}(\hat{n}; \hat{\Phi}), b) \odot S + \mathcal{R}_{\Phi}, \quad (1)$$

where \odot is element-wise multiplication, \mathcal{R}_s and \mathcal{R}_{Φ} are regularization terms for the SDF and parameters of \mathcal{F} . More details are provided in the Methods. The NFH-SEM training pipeline is highly efficient, with all three training stages for a single sample taking only about 2 minutes on an NVIDIA RTX 4090 GPU. After training, a high-quality 3D surface model can be extracted from the neural field at arbitrary resolution⁴³, with significantly improved accuracy and surface detail (Fig. 1e).

Surface Reconstruction of Microstructures using NFH-SEM

To evaluate the effectiveness of NFH-SEM in reconstructing 3D surface models across various microstructures, we collected a multi-view, multi-detector SEM dataset covering a wide range of samples with diverse geometric features. This dataset includes complex microstructures fabricated via the TPL technique, as well as peach pollen and SiC particle surfaces. We compared our NFH-SEM with two existing SEM 3D reconstruction approaches. The first one is a representative SfM-based software, Agisoft Metashape. Many prior works^{9–11} have adopted this approach to reconstruct 3D models from multi-view SE images. We also used this approach as the SfM initialization in our pipeline. The second is a PS-based method, which estimates surface gradients from 4Q-BSE images¹⁵ and then reconstructs the 3D surface model via global least-squares integration^{44–46}.

Reconstruction of Two-photon Lithography Microstructures. TPL^{47–49} is a high-resolution additive manufacturing

technique that leverages two-photon absorption photopolymerization of resins to fabricate complex 3D microstructures, with broad applications in optical devices⁵⁰, microrobotics⁵¹, and biomedical scaffolds⁵². Accurate 3D reconstruction of printed structures is essential for optimizing TPL process parameters, improving printing quality, and ensuring structural reliability. We fabricated three intricate TPL microstructures named Wukong, Lucy, and Lion. These samples exhibit intricate surface textures, large height variations, and substantial shadowing in 4Q-BSE images, posing significant challenges for PS-based methods. In addition, smooth and textureless regions on the printed surfaces also limit the effectiveness of SfM-based methods. As shown in Fig. 2d–f, the SfM baseline captures the coarse overall geometry but fails to accurately reconstruct smooth base surfaces and misses fine structural features such as the hair strands of Wukong (Fig. 2d) and Lion (Fig. 2f). These details appear overly smooth or entirely absent. While capable of recovering surface textures, the PS method suffers from global shape distortions caused by erroneous gradient estimates in shadowed or steep regions. By contrast, NFH-SEM (Fig. 2j–l) reconstructs both global geometry and local surface detail with high fidelity. It preserves fine textures on complex features while accurately modeling textureless, smooth surfaces. Notably, the Lucy model displays distinct layering structures corresponding to the 500 nm step size of the TPL printing process (see the Methods for more TPL printing details). NFH-SEM estimates the layer height of 478 nm (Fig. 2k), closely matching the ground truth. In contrast, the PS method yields a larger error of 576 nm (Fig. 2h), while SfM fails to capture the layering entirely (Fig. 2e). These results highlight the strength of NFH-SEM

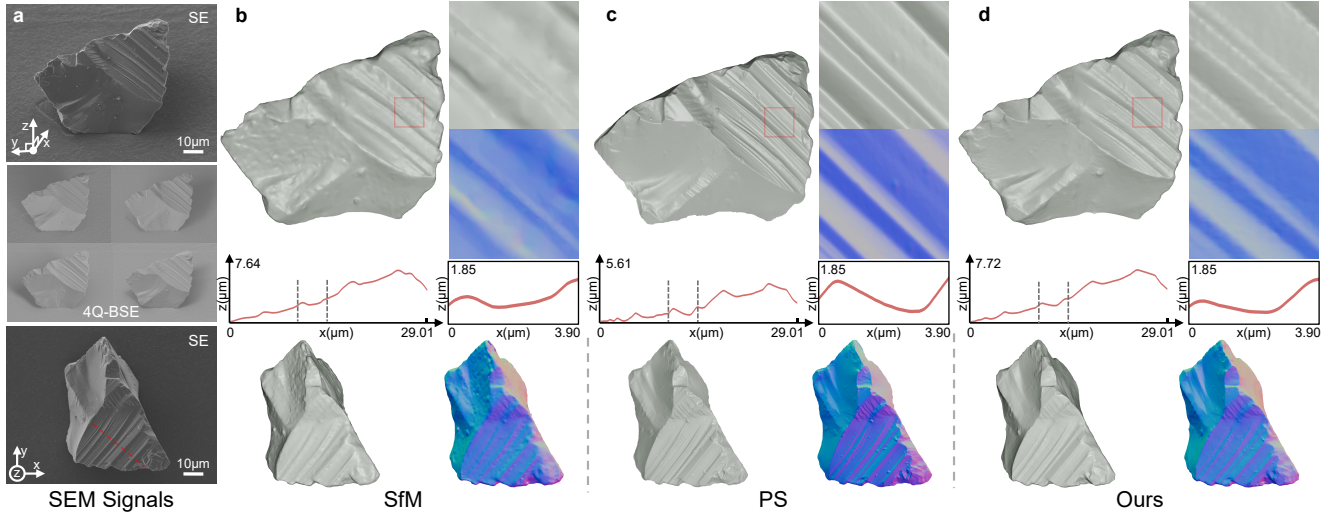


Fig. 4 | Reconstruction comparison on silicon carbide. **a**, Side-view SE and 4Q-BSE images, and a top-view SE image of the silicon carbide particle. **b**, Reconstruction using the SfM method. **c**, Reconstruction using the PS method. **d**, Reconstruction using the proposed NFH-SEM. In **b–d**, differences in fracture patterns are highlighted with red boxes and cross-sectional views. The bottom row shows top views of the reconstructed models along with their surface normals. Additional visualizations are provided in Supplementary Video 3.

in simultaneously addressing the limitations of SfM and PS, leading to more complete and accurate 3D reconstructions of complex microstructures.

Reconstruction of peach pollen. We further validate NFH-SEM on reconstructing the pollen surface. Pollen is a widely studied biological structure with intricate surface features critical to disciplines such as plant taxonomy⁵³, pollination mechanism studies⁵⁴, and biomimetic designs⁵⁵. In particular, we selected Okubo peach pollen⁵⁶, whose surface exhibits densely packed yet shallow textures (Fig. 3a). These microstructures are believed to facilitate adhesion to insect pollinators⁵⁷ and play a role in species identification⁵⁸. As shown in Fig. 3b, the SfM reconstruction produces an overly smooth surface, missing the detailed texture patterns characteristic of the pollen grain. On the other hand, the PS method represents the surface using a single-valued height map, which fails to capture the complete sidewall of the pollen grain (Fig. 3c). This is also an inherent limitation of current hybrid methods^{25,26} that rely on the same height map representation. Moreover, the surface textures in the PS results appear distorted and deviate significantly from the SEM images. In contrast, NFH-SEM leverages the neural field’s ability to better represent intricate microstructures and effectively integrates gradient cues from multi-view 4Q-BSE images, accurately reflecting surface variations. As shown in Fig. 3d, the reconstructed pollen surface closely aligns with SEM images, faithfully preserving biologically relevant morphological features.

Reconstruction of silicon carbide. Next, we evaluate NFH-SEM on an SiC microparticle. As an advanced ceramic material with outstanding hardness, chemical inertness, and high thermal conductivity, SiC⁵⁹ is widely used

in electronics, biomedicine, and photocatalysis. The SiC particles used in our study were produced by mechanically fracturing SiC crystals⁶⁰, resulting in surfaces that exhibit typical fracture-induced features. As shown in Fig. 4a, these surfaces include smooth, textureless fracture planes, densely layered step-like patterns, and sharp, irregular edges. This combination of geometric complexity poses significant challenges for existing SEM 3D reconstruction methods. The SfM method, which relies on feature matching, performs poorly on the smooth, textureless fracture planes, introducing substantial geometric noise and distortions (Fig. 4b). Furthermore, the repetitive step structures lead to matching ambiguities, resulting in blurred and inaccurate reconstructions in those regions, as highlighted in the red box. The PS method (Fig. 4c), which integrates surface gradients to recover geometry, fails to handle abrupt height discontinuities across the fractured surfaces and produces a distorted overall shape. As shown in Fig. 4d, NFH-SEM successfully reconstructs these complex structures, including distinct step patterns, smooth fracture planes, and sharp edges, with high fidelity to the SEM observations. Cross-sectional views further highlight these differences. SfM produces smoothed step corners, while PS yields lower overall heights, failing to capture the gradual elevation changes due to accumulated errors in gradient integration. On the contrary, NFH-SEM preserves both the global geometry and fine structural details in the cross-section. These results underscore the superior capability of NFH-SEM in reconstructing the microparticle with intricate fracture features. Such precise 3D characterization is critical for applications in material failure analysis and fracture mechanics research^{61–63}.

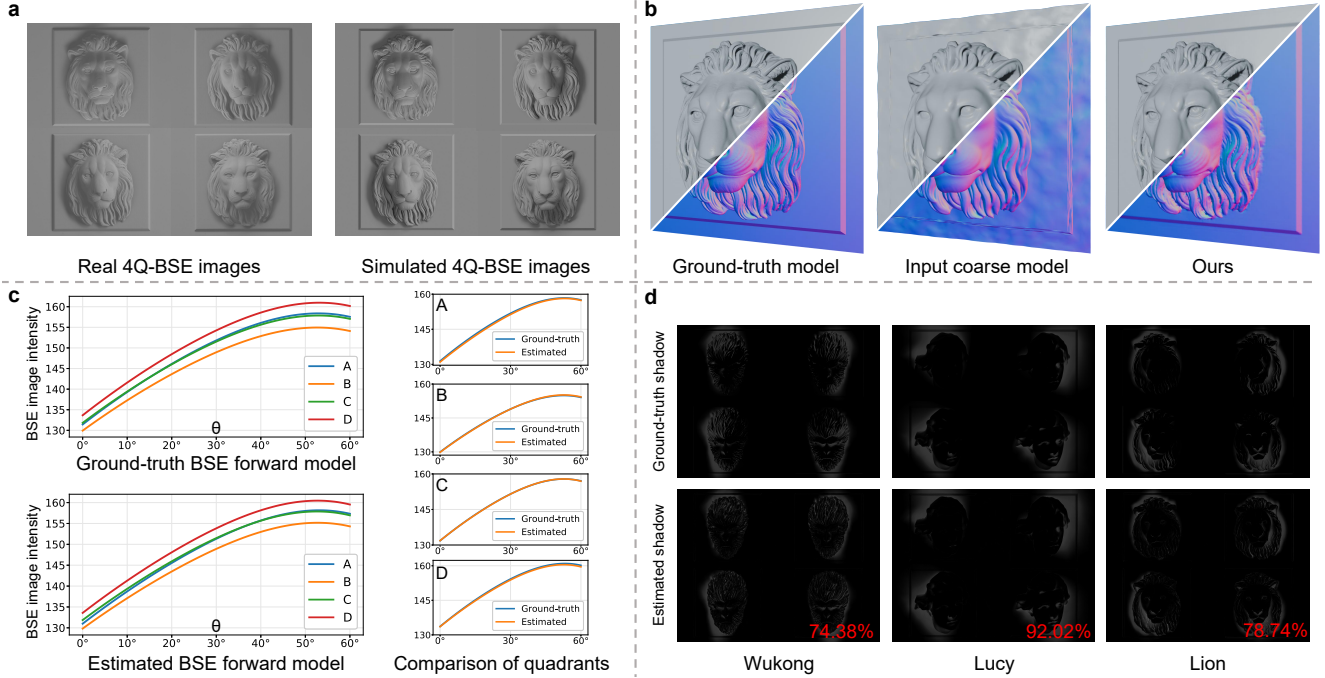


Fig. 5 | Simulation experiments. **a**, Comparison between real and simulated 4Q-BSE images. **b**, Comparison among the ground-truth model, the input coarse model, and the NFH-SEM reconstruction. **c**, Comparison of the relationship between incident angle θ and BSE image intensity, derived from the ground-truth and NFH-SEM-estimated BSE forward models. Curves from the four detector quadrants are shown separately and labeled *A*, *B*, *C*, and *D*. **d**, Comparison between the soft shadow maps extracted by NFH-SEM with the ground-truth shadow intensity maps used in simulation. The percentage in the bottom-right corner indicates the accuracy of the estimated shadows. See the Methods section for detailed definitions of the evaluation metrics.

Quantitative Evaluation on Simulated Dataset

To quantitatively evaluate the performance of NFH-SEM in geometric reconstruction, BSE forward modeling, and shadow separation, we constructed a simulated dataset based on computer-aided design (CAD) models used for TPL microstructure fabrication. This dataset closely replicates SEM imaging characteristics under real experimental conditions. NFH-SEM training requires a coarse initial model and multi-view 4Q-BSE images. A key step in the simulation is generating realistic 4Q-BSE images. To this end, virtual cameras were configured to match SEM scanning viewpoints. We then generated shadow-free BSE images using the forward model \mathcal{F} , with parameters pre-trained on the corresponding real data. To simulate BSE shadow effects, we used ray-tracing rendering to obtain quadrant-specific BSE shadow intensity maps. As shown in Fig. 5a, the resulting 4Q-BSE images exhibit realistic textures, shadows, and intensity distributions that closely resemble real BSE images (see also Supplementary Fig. 1). Since an accurate SE forward model is unavailable, the realistic simulation of multi-view SE images for SfM is infeasible. Instead, a coarse model was synthesized by applying blur and noise perturbation to the CAD model to approximate real SfM outputs. This coarse model then serves as the input to NFH-SEM. As illustrated in Fig. 5b, NFH-SEM

eliminates surface deformations in the coarse input and reconstructs high-fidelity surface details that match the CAD model (see the Methods section for simulation details).

We compared the quantitative results of different methods and conducted ablation studies to evaluate the effectiveness of each component in NFH-SEM. In the ablation studies, we designed four comparative experiments: Integrating PS-based gradient cues directly during training, where normal supervision is computed from gradient maps using the conventional PS method, without our learned BSE forward model (w/o BSE- \mathcal{F}); Replacing our learnable polynomial BSE forward model with the empirical formulation used in prior PS methods (w/o Poly-**R**); Assuming shared detector parameters across four BSE quadrants instead of learning separate ones in NFH-SEM (w/o 4Q-Var); Disabling shadow region masking in supervision, with training limited to the first two stages only (w/o S-Mask).

Table 1 and Table 2 report the accuracy of the reconstructed geometry. The PS method exhibits large geometric errors due to the integration of inaccurate gradients, which distort the global structure and introduce significant surface normal deviations. Directly using such erroneous gradients as supervision for the neural field (w/o BSE- \mathcal{F}) further degrades reconstruction quality. Compared to the input coarse model, NFH-SEM significantly improves accuracy,

reducing depth error by 26.6% and normal error by 52.9%. The BSE forward model defines the mapping from surface normals to BSE image intensities and affects the reliability of the inferred gradient information backpropagated to the neural field. As shown in Table 3, simplified forward models used in the w/o Poly-**R** and w/o 4Q-Var settings result in higher errors. These forward model inaccuracies also impair the geometry learned by the neural field, as reflected in Table 1 and Table 2. By contrast, the complete NFH-SEM learns the accurate forward model for all four BSE quadrants, closely matching the ground-truth curves (Fig. 5c). Moreover, the soft shadow maps separated by NFH-SEM achieve a high mean accuracy of 81.71% (Fig. 5d), preventing shadow artifacts from corrupting the learned geometry or forward model. As a result, compared to the w/o S-Mask setting, NFH-SEM achieves higher accuracy in both BSE forward modeling and geometry reconstruction. These results demonstrate the effectiveness of each NFH-SEM component. Quantitative metric definitions are provided in the Methods section. Additional qualitative results using the same ablation setup on real TPL data are presented in the ‘Ablation Studies on TPL Microstructures’ section of the Supplementary Information.

Depth MAE ↓	Wukong	Lucy	Lion	Average
Input coarse model	1.12	0.60	0.64	0.79
PS	6.91	18.39	5.91	10.40
Ours (w/o BSE- \mathcal{F})	1.68	2.26	1.36	1.77
Ours (w/o Poly- R)	1.01	0.60	0.52	0.71
Ours (w/o 4Q-Var)	0.95	0.49	0.52	0.65
Ours (w/o S-Mask)	0.90	0.58	0.54	0.67
Ours	0.86	0.44	0.44	0.58

Table 1 | Comparison of depth accuracy across reconstruction methods. Mean absolute error (MAE) of the estimated depth maps for each method. All reconstructed models are scaled to match the physical dimensions of the TPL-fabricated microstructures. Therefore, errors are reported in micrometers (μm). The best results are highlighted in bold.

Normal angle error ↓	Wukong	Lucy	Lion	Average
Input coarse model	10.12	5.96	7.46	7.85
PS	11.72	15.54	11.70	12.99
Ours (w/o BSE- \mathcal{F})	7.99	7.20	7.26	7.48
Ours (w/o Poly- R)	6.28	2.45	4.30	4.34
Ours (w/o 4Q-Var)	5.95	1.85	3.94	3.91
Ours (w/o S-Mask)	6.28	2.29	4.50	4.36
Ours	5.78	1.60	3.71	3.70

Table 2 | Comparison of surface normal accuracy across reconstruction methods. Mean angular error (in degrees) of the estimated surface normal maps for each method. The best results are highlighted in bold.

BSE model error ↓	Wukong	Lucy	Lion	Average
Ours (w/o Poly- R)	7.60	7.11	6.77	7.16
Ours (w/o 4Q-Var)	1.28	1.39	1.39	1.35
Ours (w/o S-Mask)	1.10	0.33	0.40	0.61
Ours	0.36	0.21	0.25	0.27

Table 3 | Comparison of the accuracy of the learned BSE forward model. Errors between the estimated mappings from surface normals to BSE image intensities (pixel range 0–255) and the ground-truth mappings used in the simulation. Errors are reported in pixel intensity units. The best results are highlighted in bold.

Discussion

NFH-SEM is a novel neural field-based hybrid SEM 3D reconstruction framework designed to recover complex microstructures from multi-view, multi-detector 2D SEM images. It offers several key advantages over prior methods. First, NFH-SEM can effectively extract and integrate geometric and photometric cues into a unified, coordinate-based neural field. This continuous representation enables better capture of intricate surface features while supporting mesh extraction at arbitrary resolution. Second, NFH-SEM achieves self-calibration of detector parameters by embedding them into a differentiable BSE forward model and jointly optimizing with the neural field end-to-end. Therefore, NFH-SEM does not require a calibration process and thus simplifies usage. Third, NFH-SEM can separate shadows in SEM images, effectively mitigate their impact on surface gradient estimation, and improve reconstruction accuracy. Our experiments demonstrate high-fidelity reconstructions across diverse samples, including the TPL-fabricated microstructures, the peach pollen, and the SiC particle, highlighting the generalization and broad applicability of NFH-SEM. Moreover, simulation studies quantitatively validate the effectiveness of each component in the NFH-SEM pipeline. Although our experiments use data from a 4Q-BSE detector, a standard configuration in many SEM systems, NFH-SEM is also flexible and compatible with alternative detector setups, such as using data from a 3Q-BSE detector (see the ‘Results on 3Q-BSE Data’ section in the Supplementary Information), underscoring its adaptability to different hardware environments.

The error in extracting surface gradients from SEM images primarily comes from deviations between the actual electron distribution and the idealized physical model. As in prior methods, our approach estimates surface gradients from 4Q-BSE images under the assumption of the Lambertian distribution of BSE signals. However, in addition to the shadowing effects already considered in NFH-SEM, real-world SEM imaging is also influenced by phenomena such as edge effects and charging effects¹⁷. Both introduce deviations from the ideal Lambertian model. Moreover, charging artifacts also introduce brightness variations and distortions in SEM images¹, which in turn degrade feature

matching and reconstruction accuracy in multi-view methods. These effects are also not accounted for in conventional SfM-based pipelines. Future work will focus on developing more accurate gradient estimation strategies from BSE data that move beyond the Lambertian assumption, as well as exploring robust correction techniques to mitigate the impact of charging artifacts in SEM imaging.

Methods

Multi-View and Multi-Detector SEM Imaging

All experiments were conducted using a ZEISS Gemini 560 SEM system equipped with a field emission gun and controlled via the ZEISS SmartSEM software. Samples were mounted on a motorized stage and sequentially rotated under SmartSEM control to enable multi-view imaging. For each sample, the stage was tilted along two orthogonal axes in 5° increments, ranging from -45° to $+45^\circ$, resulting in 37 distinct viewing directions. At each viewpoint, an SE image was acquired using the Everhart-Thornley detector located at the side of the chamber. We also used the pneumatically retractable BSE detector inserted beneath the objective lens to capture four BSE images from its four outer quadrants. We recorded all SEM images at a resolution of 1024×768 pixels. To ensure high image quality and operational safety, the accelerating voltage was set between 5 and 7 kV, and the working distance was maintained between 7 and 12 mm to avoid collisions between the stage and objective lens during tilting. Before data acquisition, we optimized the SEM parameters for each sample to enhance image clarity and suppress charging artifacts. Once optimized, all SEM parameters, including accelerating voltage, working distance, magnification, brightness, and contrast, were held constant throughout the multi-view imaging.

To improve the efficiency of multi-view and multi-detector data acquisition, we utilized the compucentric function in SmartSEM, enabling the SEM to maintain focus on the sample as the stage tilts or rotates. To enable this function, the rotation center and its distance to the sample surface were determined following SmartSEM’s operational guidelines. With this information, the software automatically computed the stage offsets after each tilt or rotation, ensuring the sample remained centered in the image. Furthermore, we packaged all data acquisition processes into a single automated macro script, utilizing SmartSEM’s macro command interface to realize multi-detector imaging and stage movements. Therefore, operator intervention was limited to occasional manual corrections for accumulated stage positioning drift, resulting in a low manual workload for the entire data acquisition process.

NFH-SEM Reconstruction Pipeline

Neural field architecture. The neural field \mathcal{M} consists of a multi-resolution hash table and an MLP network, designed

to map a 3D coordinate to its corresponding SDF value. The learnable parameters Θ include both hash table parameters and MLP weights. Each 3D point is first encoded using multi-resolution hashing⁴², a technique that significantly accelerates training and inference of neural fields. We adopt a 16-level hash table, with each level contributing a 2D feature, yielding a concatenated 32-dimensional feature vector. This hash-encoded vector is then concatenated with the 3D coordinate and passed as input to the MLP, a shallow, fully connected network with one hidden layer of size 64 and the ReLU activation. The MLP outputs a single SDF value for the queried 3D coordinate. This neural field representation is built upon an open-source PyTorch⁶⁴ implementation⁶⁵ of NeuS²⁸. The SDF is then converted into a density value using an unbiased and occlusion-aware weighting function²⁸. The point normal is obtained by computing the gradient of the SDF. Finally, volume rendering is performed along each camera ray to compute surface intersection depths \hat{z} and normals \hat{n} .

SfM initialization. We use the standard 3D reconstruction pipeline provided by Agisoft Metashape v2.1.2 (Agisoft LLC)⁹⁻¹¹, which takes multi-view SE images as input to generate a 3D model of the sample along with the corresponding virtual camera parameters for each view. This reconstructed model represents the SfM baseline in our experiments and also serves as the initial geometry for the NFH-SEM pipeline. Moreover, each vertex in the reconstructed mesh carries a confidence value, which reflects the software’s estimation of the local reconstruction reliability. Given the reconstructed mesh and camera parameters, we computed a depth map z and an associated confidence map w for each view. They are used to supervise the neural field’s geometric representation by minimizing a confidence-weighted depth loss:

$$\mathcal{L}_{\text{depth}} = \frac{1}{M} \sum_j w_j |\hat{z}_j - z_j|, \quad (2)$$

where M is the batch size and j indexes individual rays. This loss suppresses the influence of uncertain regions in the SfM reconstruction and provides a coarse geometric prior for the neural field.

SDF regularization. Additionally, we apply a regularization term \mathcal{R}_s to all sampled points along the rays,

$$\mathcal{R}_s = \frac{1}{MN} \sum_{j,k}^{M,N} (\|\nabla s_{jk}\| - 1)^2, \quad (3)$$

encouraging the SDF to have a unit-norm gradient, ∇s , where N is the number of sample points along each ray and k is its index. The SDF gradient also represents the predicted normal at each point. This regularization⁴¹ is a standard constraint in SDF-based neural field representations and ensures that the network learns a valid SDF.

PS reconstruction of 4Q-BSE images. PS-based SEM 3D reconstruction methods are built upon the assumption that

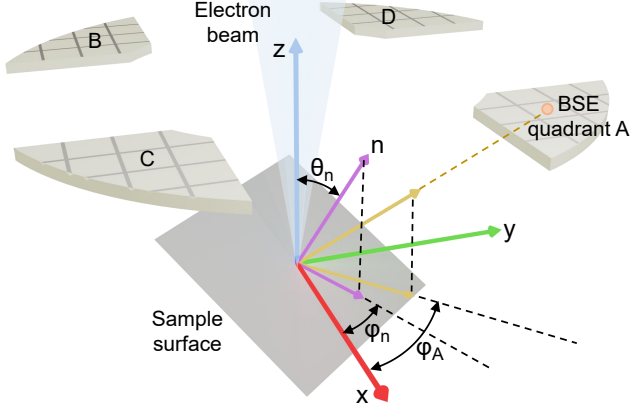


Fig. 6 | Definition of angles in the learnable BSE forward model. Key geometric angles involved in the emission of BSE from the sample surface and its detection by the 4Q-BSE detector.

BSE signals emitted from the sample surface follow the Lambertian angular distribution¹. Under this assumption, the signal intensity I_i detected by the quadrant i of the BSE detector, $i \in \{A, B, C, D\}$, can be modeled as a function of the local surface normal n ^{15,66}:

$$I_i(n) = \mathbf{R}_0(\theta_n) [d_i \cos(\varphi_i - \varphi_n) \sin(\theta_n) + c_i \cos(\theta_n)], \quad (4)$$

where the angles θ and φ , as illustrated in Fig. 6, define the relationship between the surface normal and the directions toward the quadrants. Parameters c and d are related to the configuration of the BSE detector. The scaling of signal intensity due to the electron beam current and the emission coefficient is also incorporated into c and d ⁶⁶. \mathbf{R}_0 models the emission magnification as a function of the incidence angle θ , and is often chosen as the inverse cosine of θ in prior works:

$$\mathbf{R}_0(\theta) = \sec(\theta). \quad (5)$$

This allows the sine and cosine terms in Eq. (4) to cancel out, yielding the following expression for the signal:

$$I_i(n) = d_i \cos(\varphi_i - \varphi_n) \tan(\theta_n) + c_i. \quad (6)$$

This expression forms the theoretical basis of PS-based SEM reconstruction methods¹⁵⁻¹⁸. Given the symmetric layout of the 4Q-BSE detector along two orthogonal axes, we define the X-axis as the line connecting quadrants A and B, with $\varphi_A = \varphi_B + \pi$. Moreover, a core assumption of PS methods is that all quadrants share the same parameters c and d . Therefore, the surface gradient along the X-direction can be computed from intensity measurements:

$$\frac{I_A(n) - I_B(n)}{I_A(n) + I_B(n)} = \frac{d}{c} \tan \theta_n \cos \varphi_n = \frac{d}{c} \frac{\partial z}{\partial x}. \quad (7)$$

Similarly, the Y-direction gradient can be obtained using quadrants C and D. However, in practice, the orientation of the detector quadrants may not align with the SEM image axes, depending on the installation angle of the BSE detector and the SEM scan direction. Therefore, the gradient estimated in Eq. (7) must be transformed into the image coordinate system. Surface reconstruction is then performed by

integrating the image gradient field. We use the MATLAB toolbox grad2Surf v1.0⁴⁴⁻⁴⁶, which applies a global least-squares integration method, to recover the sample topography from the image gradients. It is important to note that the ratio d/c acts as a scaling factor for the reconstructed height range. Prior PS methods require complex calibration procedures with reference samples to estimate this ratio. In our experiments, we obtain the PS baseline result by scaling its height range to match that of the SfM reconstruction, enabling a fair comparison between different methods.

Learnable BSE forward model and supervision. We do not directly use the surface gradients computed from Eq. (7) as supervision (as in the w/o BSE- \mathcal{F} setting in ablation studies). Instead, we construct a learnable BSE forward model and minimize the difference between the estimated and input 4Q-BSE images. However, in practice, we find that Eq. (6) fails to accurately capture the relationship between surface normals and image intensities in real 4Q-BSE data (as in the w/o Poly-R setting in ablation studies). To improve modeling accuracy, we replace the emission function \mathbf{R}_0 with a more flexible, learnable fourth-order polynomial:

$$\mathbf{R}(\theta) = 1 + p_1\theta + p_2\theta^2 + p_3\theta^3 + p_4\theta^4. \quad (8)$$

Our forward model, which maps surface normals to BSE intensities, is denoted as \mathcal{F} :

$$\mathcal{F}_i(n; \Phi) = \mathbf{R}(\theta_n) [d_i \cos(\varphi_i - \varphi_n) \sin(\theta_n) + c_i \cos(\theta_n)] + e_i. \quad (9)$$

Because the captured BSE images are not the raw detector signal intensities, here, we introduce an additional parameter e , accounting for intensity shifts due to brightness adjustments. As in previous works²⁵, we assume a homogeneous electron emission coefficient, which is reasonable under our coated samples and low accelerating voltage conditions¹. Moreover, we account for inter-quadrant differences¹⁷ and do not constrain their parameters to be identical. Therefore, our forward model \mathcal{F} contains a total of 16 learnable parameters, $\Phi = \{c, d, e, p\}$, where c, d and e are different in each quadrant, and p are four polynomial parameters. The BSE loss is defined as the mean absolute error (MAE) between the input 4Q-BSE images b and the estimated BSE images obtained by applying \mathcal{F} to the surface normal \hat{n} inferred from the neural field:

$$\mathcal{L}_{\text{BSE}} = \frac{1}{4M} \sum_i^{A,B,C,D} \sum_j^M S_{ij} \odot \left| \mathcal{F}_i(\hat{n}_j; \hat{\Phi}) - b_{ij} \right|. \quad (10)$$

S is the shadow mask, where shadowed regions are 0. In practice, we observe that regions where \mathcal{F} significantly deviates from the real BSE image b closely align with shadowed regions, as these areas cannot be modeled as functions of the surface normal. We thus exclude such pixels from supervision using the condition $S_i = (|\mathcal{F}_i(\hat{n}; \hat{\Phi}) - b_i| < \alpha d_i)$. The shadow threshold is determined by the parameter d for each quadrant during training. Since this parameter primarily controls the sensitivity of BSE intensity to surface

topography, the threshold is set proportional to d to avoid misclassifying intensity variations due to local geometric changes as shadows. We set α to 0.25 for the TPL microstructures and 0.5 for the pollen and SiC samples. Moreover, many studies^{17,19} have reported that the Lambertian assumption becomes unreliable at large tilt angles. Therefore, we restrict the application of \mathcal{L}_{BSE} to regions with surface tilt angle θ less than 60 degrees. Nevertheless, due to the multi-view scanning strategy in NFH-SEM, regions with high tilt angles in one view often appear at lower tilt in others. As demonstrated in our experiments, BSE information from multiple perspectives collectively provides comprehensive supervision of the microstructure geometry. **BSE forward model regularization.** Our BSE forward model accounts for parameter differences¹⁷ across the four quadrants of the BSE detector. In practice, the properties of these quadrants are expected to be similar. To regularize the forward model and prevent overfitting, we introduce a penalty term \mathcal{R}_Φ that penalizes variance among corresponding parameters across quadrants:

$$\mathcal{R}_\Phi = \text{Var}(c) + \text{Var}(d) + \text{Var}(e), \quad (11)$$

where $\text{Var}(\cdot)$ denotes the variance computed across the four quadrant-specific values within each parameter group. This encourages quadrant consistency while avoiding suboptimal convergence.

Training of NFH-SEM. Rather than optimizing all loss components simultaneously, we adopt a staged training strategy for NFH-SEM to ensure stability and efficiency. The training is divided into three consecutive stages. In the first stage, the neural field is supervised solely using SfM depth information by minimizing $\mathcal{L}_{\text{depth}}$ and the regularization term \mathcal{R}_s . This step initializes the SDF representation in the neural field with a coarse geometry prior, improving convergence stability. In the second stage, we introduce surface gradient cues from 4Q-BSE images into the neural field and jointly optimize the model \mathcal{F} by minimizing \mathcal{L}_{BSE} and \mathcal{R}_Φ . At this stage, shadow masking is not yet applied, since the surface normals and parameters Φ are not sufficiently optimized to reliably detect shadowed regions. In the third stage, we activate dynamic shadow masking in \mathcal{L}_{BSE} to exclude shadow regions from supervision. This refinement stage improves both the accuracy of the reconstructed microstructure geometry and the model \mathcal{F} . The overall training objective \mathcal{L} is defined as:

$$\mathcal{L} = \begin{cases} \lambda_1 \mathcal{L}_{\text{depth}} + \lambda_2 \mathcal{R}_s, & 0 < \beta \leq t_1, \\ \lambda_1 \mathcal{L}_{\text{depth}} + \lambda_2 \mathcal{R}_s + \lambda_3 \mathcal{L}_{\text{BSE}}(1) + \lambda_4 \mathcal{R}_\Phi, & t_1 < \beta \leq t_2, \\ \lambda_1 \mathcal{L}_{\text{depth}} + \lambda_2 \mathcal{R}_s + \lambda_3 \mathcal{L}_{\text{BSE}}(S) + \lambda_4 \mathcal{R}_\Phi, & t_2 < \beta \leq t_3. \end{cases} \quad (12)$$

Here, β denotes the training step, with stage boundaries $t_1 = 1000$, $t_2 = 2000$, and $t_3 = 3000$. $\mathcal{L}_{\text{BSE}}(1)$ and $\mathcal{L}_{\text{BSE}}(S)$ represent the BSE loss computed without and with shadow masking, respectively. We set λ_1 to 0.5 for the TPL samples and 0.1 for the pollen and SiC samples, while λ_2 , λ_3 , and λ_4 are set to 0.1, 1.0, and 1.0 across all samples.

The network was optimized using the Adam optimizer⁶⁷ with a learning rate of 0.01. At each iteration, 256 rays were randomly sampled, with 1024 points along each ray. Training was conducted on a workstation equipped with an AMD 5950X CPU, NVIDIA RTX 4090 GPU, and 128 GB RAM. The entire training process of one microstructure consists of 3000 iterations and takes only about 2 minutes, demonstrating the high efficiency of our method.

After training the neural field, we discretize the space into a $512 \times 512 \times 512$ voxel grid and infer the SDF value at each vertex. These SDF values are then converted into meshes using the Marching Cubes algorithm⁴³ to generate the visualized 3D models shown in our experiments. Since the neural field provides a continuous representation of space, SDF values can be inferred at arbitrary locations, enabling users to extract models at any desired resolution.

Fabricating the Two-Photon Lithography Structures

Microstructures were fabricated using the commercial photoresist IP-S (Nanoscribe GmbH), which was dispensed onto an indium tin oxide-coated glass substrate (25 mm \times 25 mm \times 0.7 mm, Nanoscribe GmbH). A commercial direct laser writing system (Photonic Professional GT2, Nanoscribe GmbH), equipped with a 780 nm femtosecond laser (80 MHz repetition rate, 80–100 fs pulse duration) and a $25\times$ objective lens with a numerical aperture (NA) of 0.8, was employed for the 3D printing of microstructures. STL models were processed in Describe v2.7 (Nanoscribe GmbH) to generate executable job files, with the slicing and hatching distances set to 500 nm and 400 nm, respectively. We set printing parameters with a laser power of 50 mW and a scanning speed of 50,000 $\mu\text{m/s}$. These job files were then transferred to NanoWrite v1.8 (Nanoscribe GmbH) to initiate the writing process. After printing, the microstructures were developed in propylene glycol methyl ether acetate (PGMEA) for 20 minutes, followed by rinsing in isopropyl alcohol (IPA) for 5 minutes at room temperature to remove unpolymerized photoresist. Prior to SEM imaging, the printed microstructures on the substrate were sputter-coated with a thin platinum layer using an ion sputter coater (GVC-2000, Gewei Instrument) at 15 mA for 60 seconds.

Preparing the Pollen and Silicon Carbide Samples

The Okubo peach pollen was sourced from Dangshan County Orchard Farm (China). The micro-scale SiC powder was purchased from Beesley New Materials (Suzhou) Co., Ltd. (China). It was produced via a high-temperature reaction between silica and petroleum coke, followed by crushing and classification to obtain particles with an average diameter of approximately 45 μm . Both samples were prepared using the same procedure. They were mounted on 9.5 mm aluminum pin stubs using carbon conductive adhesive tabs and coated with gold using an E-1010 ion sputter

coater (Hitachi) at a 15 mA current for 60 seconds, effectively preventing charging artifacts during SEM imaging.

Constructing the Simulated Dataset

We constructed a simulated dataset for quantitative evaluation based on the STL models used to fabricate the microstructures in our TPL experiments. To simulate the multi-view SEM imaging setup, virtual cameras were placed in Blender v4.1 at the same tilt and rotation angles as in our real experiments. We then applied modifiers to the STL models in Blender, introducing surface blur and noise. From these degraded meshes, we extracted depth maps for each virtual viewpoint to serve as initialization for NFH-SEM. All corresponding depth confidence values were uniformly set to 0.2. The primary goal of the simulation was to closely approximate the appearance of real-world 4Q-BSE images. To achieve this, we computed shadow-free BSE intensities using our forward model $\mathcal{F}(\bar{n}; \bar{\Phi})$, where \bar{n} denotes the surface normal maps derived from the original STL models, and $\bar{\Phi}$ represents BSE forward model parameters obtained from NFH-SEM reconstructions of real TPL samples. A critical component of the BSE image is the soft shadowing effect arising from the self-occlusion of the sample geometry. Since BSE shadow formation resembles a rendering scenario in which quadrants act as area light sources, and the electron beam serves as the viewing direction, we simulated these shadows in Blender by placing four quadrant-shaped area lights in fixed poses relative to the camera. Shadow intensity maps $\bar{\psi}$ were rendered using the Blender Cycles render engine. Moreover, to replicate the noise level of real BSE images, we estimated the pixel-wise standard deviation ($\sigma = 0.9142$ in our case) from a flat region of the TPL microstructure. This value was used to generate additive Gaussian noise $\mathcal{N}(0, \sigma^2)$.

$$b' = \mathcal{F}(\bar{n}; \bar{\Phi}) - \bar{\psi} + \mathcal{N}(0, \sigma^2). \quad (13)$$

Finally, by combining the shadow-free intensity maps, the rendered shadow maps, and the synthesized noise, we obtained the simulated 4Q-BSE images b' with high consistency with real-world 4Q-BSE images.

Ablation Study Configurations

In the direct gradient fusion implementation (w/o BSE- \mathcal{F}), 4Q-BSE images from each viewpoint are first converted to gradients using Eq. (7). The loss is computed as the MAE between these gradients and the surface normals predicted by the neural field. The scale ratio d/c is treated as a learnable parameter and optimized during training. In the w/o Poly-R setting, Eq. (6) is adopted as the BSE forward model, where each quadrant is assigned a separate set of learnable parameters c and d . In the w/o 4Q-Var setting, all four quadrants share a single set of parameters c , d , and e , thereby ignoring subtle inter-quadrant variations. In the w/o S-Mask configuration, the shadow mask S is not computed. Training is limited to the first two stages of Eq. (12), with

the second stage covering the iteration range from t_1 to t_3 . The total number of training iterations remains unchanged.

Quantitative Metrics

The depth error $\mathcal{E}_{\text{depth}}$ (Table 1) is defined as the MAE between the estimated depth \hat{z} and the ground-truth depth \bar{z} ,

$$\mathcal{E}_{\text{depth}} = \frac{1}{PQ} \sum_u^P \sum_v^Q |\bar{z}_{uv} - \hat{z}_{uv}|, \quad (14)$$

where P is the number of viewpoints with index u , and Q is the number of pixels per image with index v . The normal error $\mathcal{E}_{\text{normal}}$ (Table 2) is computed as the angular difference between the estimated normal \hat{n} and the ground-truth normal \bar{n} , where $\text{degrees}(\cdot)$ converts from radians to degrees.

$$\mathcal{E}_{\text{normal}} = \frac{1}{PQ} \sum_u^P \sum_v^Q \text{degrees}(\arccos(\bar{n}_{uv} \cdot \hat{n}_{uv})). \quad (15)$$

We evaluate the accuracy of the BSE forward model $\mathcal{F}^{\hat{\Phi}}$ with learned parameters $\hat{\Phi}$, by comparing it to the ground-truth model $\mathcal{F}^{\bar{\Phi}}$ used to generate the simulated dataset:

$$\mathcal{E}_{\text{BSE}} = \frac{1}{4T} \sum_i^{A,B,C,D} \sum_q^T \left| \mathcal{F}_i(\theta_q, \varphi_i; \bar{\Phi}) - \mathcal{F}_i(\theta_q, \varphi_i; \hat{\Phi}) \right|. \quad (16)$$

By fixing the input φ to the quadrant directions φ_i , each quadrant’s forward model depends solely on θ . We uniformly sample T angles θ_q within the 60-degree range defined by the valid supervision interval of \mathcal{L}_{BSE} , and compute the intensity difference between $\mathcal{F}^{\hat{\Phi}}$ and $\mathcal{F}^{\bar{\Phi}}$ at each θ_q . The average of these differences, \mathcal{E}_{BSE} (Table 3), reflects how accurately NFH-SEM has learned the BSE forward model.

After training, shadow-free 4Q-BSE images can be computed using the estimated surface normals \hat{n} and the learned model $\mathcal{F}^{\hat{\Phi}}$. By subtracting the input BSE images from the shadow-free images, we obtain the estimated BSE shadow intensity maps, $\hat{\psi} = \left| \mathcal{F}(\hat{n}; \hat{\Phi}) - b' \right|$. These extracted shadows are not incorporated into the neural field geometry or the forward model \mathcal{F} , demonstrating NFH-SEM’s ability to disentangle shadows in BSE images. Given the ground-truth shadow intensities $\bar{\psi}$, we define a quantitative metric to assess shadow estimation accuracy:

$$\mathcal{S}_{\text{shadow}} = 100 \times \left(1 - \frac{1}{4P} \sum_i^{A,B,C,D} \sum_u^P \frac{\sum_v^Q |\bar{\psi}_{iuv} - \hat{\psi}_{iuv}|}{\sum_v^Q (\bar{\psi}_{iuv} + \hat{\psi}_{iuv})} \right). \quad (17)$$

Since shadows in BSE images are soft and lack sharp boundaries, and stronger shadows have a greater negative impact on reconstruction, we compute the pixel-wise intensity difference between the estimated and ground-truth shadow maps. This difference is normalized by the total intensity sum of both maps. The resulting shadow accuracy score, $\mathcal{S}_{\text{shadow}}$, is expressed as a percentage, with higher values indicating more accurate shadow estimation.

References

- [1] Reimer, L. Scanning electron microscopy: physics of image formation and microanalysis. *Measurement Science and Technology* **11**, 1826–1826 (2000).
- [2] Suga, M. *et al.* Recent progress in scanning electron microscopy for the characterization of fine structural details of nano materials. *Progress in Solid State Chemistry* **42**, 1–21 (2014).
- [3] Mitragotri, S. *et al.* Accelerating the translation of nanomaterials in biomedicine. *ACS Nano* **9**, 6644–6654 (2015).
- [4] Nelson, E. C. *et al.* Epitaxial growth of three-dimensionally architected optoelectronic devices. *Nature Materials* **10**, 676–681 (2011).
- [5] Koch, K., Bhushan, B. & Barthlott, W. Diversity of structure, morphology and wetting of plant surfaces. *Soft Matter* **4**, 1943–1963 (2008).
- [6] Zhao, S. *et al.* Additive manufacturing of silica aerogels. *Nature* **584**, 387–392 (2020).
- [7] Tafti, A. P., Kirkpatrick, A. B., Alavi, Z., Owen, H. A. & Yu, Z. Recent advances in 3D SEM surface reconstruction. *Micron* **78**, 54–66 (2015).
- [8] Ball, A. D., Job, P. A. & Walker, A. E. L. SEM-microphotogrammetry, a new take on an old method for generating high-resolution 3D models from SEM images. *Journal of microscopy* **267**, 214–226 (2017).
- [9] Eulitz, M. & Reiss, G. 3D reconstruction of SEM images by use of optical photogrammetry software. *Journal of structural biology* **191**, 190–196 (2015).
- [10] Zhang, X. *et al.* Superalloys fracture process inference based on overlap analysis of 3D models. *Communications Engineering* **3**, 108 (2024).
- [11] Kozikowski, P. Extracting three-dimensional information from SEM images by means of photogrammetry. *Micron* **134**, 102873 (2020).
- [12] Schönberger, J. L. & Frahm, J.-M. Structure-from-motion revisited. In *2016 IEEE Conference on Computer Vision and Pattern Recognition (CVPR)*, 4104–4113 (2016).
- [13] Özyeşil, O., Voroninski, V., Basri, R. & Singer, A. A survey of structure from motion. *Acta Numerica* **26**, 305–364 (2017).
- [14] Iglhaut, J. *et al.* Structure from motion photogrammetry in forestry: A review. *Current Forestry Reports* **5**, 155–168 (2019).
- [15] Słówko, W. & Krysztof, M. Detector system for three-dimensional imaging in the variable pressure/environmental SEM. *Acta Physica Polonica A* **123**, 877–879 (2013).
- [16] Drzazga, W., Paluszynski, J. & Słówko, W. Three-dimensional characterization of microstructures in a SEM. *Measurement Science and Technology* **17**, 28 (2005).
- [17] Paluszynski, J. & Słówko, W. Surface reconstruction with the photometric method in SEM. *Vacuum* **78**, 533–537 (2005).
- [18] Giardino, M., Menon, D. M. N. & Janner, D. L. Regularization techniques for 3D surface reconstruction from four quadrant backscattered electron detector images. *Ultramicroscopy* **250**, 113746 (2023).
- [19] Słówko, W. Specific features of the miniature ionisation BSE multi-detector unit for 3D imaging in environmental conditions. *Micron* **126**, 102752 (2019).
- [20] Neggers, J. *et al.* Principal image decomposition for multi-detector backscatter electron topography reconstruction. *Ultramicroscopy* **227**, 113200 (2021).
- [21] Pintus, R., Podda, S. & Vanzi, M. An automatic alignment procedure for a four-source photometric stereo technique applied to scanning electron microscopy. *IEEE Transactions on Instrumentation and Measurement* **57**, 989–996 (2008).
- [22] Woodham, R. J. Photometric method for determining surface orientation from multiple images. *Optical engineering* **19**, 139–144 (1980).
- [23] Ackermann, J. & Goesele, M. A survey of photometric stereo techniques. *Found. Trends. Comput. Graph. Vis.* **9**, 149–254 (2015).
- [24] Shi, B. *et al.* A benchmark dataset and evaluation for non-lambertian and uncalibrated photometric stereo. *IEEE Transactions on Pattern Analysis and Machine Intelligence* **41**, 271–284 (2019).
- [25] Yan, S., Adegbule, A. & Kibbey, T. C. G. A hybrid 3D SEM reconstruction method optimized for complex geologic material surfaces. *Micron* **99**, 26–31 (2017).
- [26] Danzl, R. & Scherer, S. Integrating shape from shading and shape from stereo for variable reflectance surface reconstruction from SEM images. In *Proceedings 26th Workshop of the Austrian Association for Pattern Recognition (AAPR)*, 281–288 (2002).
- [27] Xie, Y. *et al.* Neural fields in visual computing and beyond. *Computer Graphics Forum* **41**, 641–676 (2022).
- [28] Wang, P. *et al.* NeuS: Learning neural implicit surfaces by volume rendering for multi-view reconstruction. *Advances in Neural Information Processing Systems* **34**, 27171–27183 (2021).
- [29] Yariv, L., Gu, J., Kasten, Y. & Lipman, Y. Volume rendering of neural implicit surfaces. *Advances in Neural Information Processing Systems* **34**, 4805–4815 (2021).
- [30] Oechsle, M., Peng, S. & Geiger, A. UNISURF: Unifying neural implicit surfaces and radiance fields for multi-view reconstruction. In *2021 IEEE/CVF International Conference on Computer Vision (ICCV)*, 5569–5579 (2021).
- [31] Mildenhall, B. *et al.* NeRF: Representing scenes as neural radiance fields for view synthesis. *Communications of the ACM* **65**, 99–106 (2021).
- [32] Barron, J. T., Mildenhall, B., Verbin, D., Srinivasan, P. P. & Hedman, P. Mip-NeRF 360: Unbounded anti-aliased neural radiance fields. In *2022 IEEE/CVF Conference on Computer Vision and Pattern Recognition (CVPR)*, 5460–5469 (2022).

- [33] Yu, A., Ye, V., Tancik, M. & Kanazawa, A. pixelNeRF: Neural radiance fields from one or few images. In *2021 IEEE/CVF Conference on Computer Vision and Pattern Recognition (CVPR)*, 4576–4585 (2021).
- [34] Zang, G., Idoughi, R., Li, R., Wonka, P. & Heidrich, W. Intratomo: Self-supervised learning-based tomography via sinogram synthesis and prediction. In *2021 IEEE/CVF International Conference on Computer Vision (ICCV)*, 1940–1950 (2021).
- [35] Liu, X. *et al.* Multi-modal neural radiance field for monocular dense SLAM with a light-weight ToF sensor. In *2023 IEEE/CVF International Conference on Computer Vision (ICCV)*, 1–11 (2023).
- [36] Shen, L., Pauly, J. & Xing, L. NeRP: Implicit neural representation learning with prior embedding for sparsely sampled image reconstruction. *IEEE Transactions on Neural Networks and Learning Systems* **35**, 770–782 (2024).
- [37] Liu, R., Sun, Y., Zhu, J., Tian, L. & Kamilov, U. S. Recovery of continuous 3D refractive index maps from discrete intensity-only measurements using neural fields. *Nature Machine Intelligence* **4**, 781–791 (2022).
- [38] Kang, I., Zhang, Q., Yu, S. X. & Ji, N. Coordinate-based neural representations for computational adaptive optics in widefield microscopy. *Nature Machine Intelligence* **6**, 714–725 (2024).
- [39] Chen, S. *et al.* Multi-view neural 3D reconstruction of micro- and nanostructures with atomic force microscopy. *Communications Engineering* **3**, 131 (2024).
- [40] Chen, S., Li, Y. & Zhang, G. OpticFusion: Multi-modal neural implicit 3D reconstruction of microstructures by fusing white light interferometry and optical microscopy. Preprint at <https://doi.org/10.48550/arXiv.2501.09259> (2025).
- [41] Gropp, A., Yariv, L., Haim, N., Atzmon, M. & Lipman, Y. Implicit geometric regularization for learning shapes. In *Proceedings of the 37th International Conference on Machine Learning*, 3789–3799 (2020).
- [42] Müller, T., Evans, A., Schied, C. & Keller, A. Instant neural graphics primitives with a multiresolution hash encoding. *ACM Transactions on Graphics (ToG)* **41**, 1–15 (2022).
- [43] Lorensen, W. E. & Cline, H. E. Marching cubes: A high resolution 3D surface construction algorithm. In *Seminal graphics: pioneering efforts that shaped the field*, 347–353 (1998).
- [44] Harker, M. & O’Leary, P. Least squares surface reconstruction from measured gradient fields. In *2008 IEEE Conference on Computer Vision and Pattern Recognition (CVPR)*, 1–7 (2008).
- [45] Harker, M. & O’Leary, P. Direct regularized surface reconstruction from gradients for industrial photometric stereo. *Computers in Industry* **64**, 1221–1228 (2013).
- [46] Harker, M. & O’Leary, P. Regularized reconstruction of a surface from its measured gradient field algorithms for spectral, tikhonov, constrained, and weighted regularization. *Journal of Mathematical Imaging and Vision* **51**, 46–70 (2015).
- [47] Harinarayana, V. & Shin, Y. Two-photon lithography for three-dimensional fabrication in micro/nanoscale regime: A comprehensive review. *Optics & Laser Technology* **142**, 107180 (2021).
- [48] Kawata, S., Sun, H., Tanaka, T. & Takada, K. Finer features for functional microdevices - micromachines can be created with higher resolution using two-photon absorption. *Nature* **412**, 697–698 (2001).
- [49] Sun, H. *et al.* Real three-dimensional microstructures fabricated by photopolymerization of resins through two-photon absorption. *Optics letters* **25**, 1110–1112 (2000).
- [50] Wang, H. *et al.* Two-photon polymerization lithography for optics and photonics: fundamentals, materials, technologies, and applications. *Advanced Functional Materials* **33**, 2214211 (2023).
- [51] Lee, H., Kim, D.-i., Kwon, S.-h. & Park, S. Magnetically actuated drug delivery helical microrobot with magnetic nanoparticle retrieval ability. *ACS applied materials & interfaces* **13**, 19633–19647 (2021).
- [52] Marino, A. *et al.* Two-photon lithography of 3D nanocomposite piezoelectric scaffolds for cell stimulation. *ACS applied materials & interfaces* **7**, 25574–25579 (2015).
- [53] Sivaguru, M., Mander, L., Fried, G. & Punyasena, S. W. Capturing the surface texture and shape of pollen: a comparison of microscopy techniques. *Plos one* **7**, e39129 (2012).
- [54] Edlund, A., Swanson, R. & Preuss, D. Pollen and stigma structure and function: The role of diversity in pollination. *Plant Cell* **16**, S84–S97 (2004).
- [55] Fan, T.-F. *et al.* Transformation of hard pollen into soft matter. *Nature Communications* **11**, 1449 (2020).
- [56] Zhang, H. *et al.* Managed bumblebees outperform honeybees in increasing peach fruit set in China: different limiting processes with different pollinators. *Plos one* **10**, e0121143 (2015).
- [57] Lin, H., Gomez, I. & Meredith, J. C. Pollenkitt wetting mechanism enables species-specific tunable pollen adhesion. *Langmuir* **29**, 3012–3023 (2013).
- [58] Evrenosoğlu, Y. & Misirli, A. Investigations on the pollen morphology of some fruit species. *Turkish Journal of Agriculture and Forestry* **33**, 181–190 (2009).
- [59] Xu, M. *et al.* Recent advances and challenges in silicon carbide (SiC) ceramic nanoarchitectures and their applications. *Materials Today Communications* **28**, 102533 (2021).
- [60] Wang, Y., Dong, S., Li, X., Hong, C. & Zhang, X. Synthesis, properties, and multifarious applications of SiC nanoparticles: A review. *Ceramics International* **48**, 8882–8913 (2022).
- [61] Pilchak, A. L. Fatigue crack growth rates in alpha titanium: Faceted vs. striation growth. *Scripta Materialia* **68**, 277–280 (2013).

- [62] Murashkin, M. *et al.* Fatigue behavior of an ultrafine-grained Al-Mg-Si alloy processed by high-pressure torsion. *Metals* **5**, 578–590 (2015).
- [63] Birenis, D. *et al.* Interpretation of hydrogen-assisted fatigue crack propagation in BCC iron based on dislocation structure evolution around the crack wake. *Acta Materialia* **156**, 245–253 (2018).
- [64] Paszke, A. *et al.* PyTorch: An imperative style, high-performance deep learning library. *Advances in neural information processing systems* **32**, 8024–8035 (2019).
- [65] Guo, Y.-C. Instant neural surface reconstruction. *Github*. <https://github.com/bennyguo/instant-nsr-pl> (2022).
- [66] Abdallah, Z., Fay, A. & Bonnet, S. 3D SEM metrology of microstructures for high volume manufacturing. In *38th European Mask and Lithography Conference (EMLC 2023)*, vol. 12802, 128020N (SPIE, 2023).
- [67] Kingma, D. P. & Ba, J. Adam: A method for stochastic optimization. Preprint at <https://doi.org/10.48550/arXiv.1412.6980> (2017).

Acknowledgements

We sincerely thank A. Ren and L. Ma for their assistance with the TPL experiments. We gratefully acknowledge the Edward J. Team for their support of the Wukong 3D model. We also thank N. Rong, J. Niu, and D. Qi of the Analysis Center of Agriculture, Life and Environment Sciences, Zhejiang University, and J. Huang of Carl Zeiss (Shanghai) Co., Ltd., for their technical support. We acknowledge the assistance of Y. Chen during the SEM experiments. We are grateful to W. Słówko for insightful discussions. This work was partially supported by the National Natural Science Foundation of China (No. 62425209).

Author information

Authors and Affiliations

State Key Lab of CAD&CG, Zhejiang University, Hangzhou 310058, China

Shuo Chen & Guofeng Zhang

Alibaba Group, Hangzhou 311121, China

Yijin Li

Analysis Center of Agriculture, Life and Environment Sciences, Zhejiang University, Hangzhou 310058, China
Xi Zheng

Contributions

S.C. conceived the idea, conducted experiments, implemented the code, and wrote the manuscript; Y.L. participated in discussions on the experimental design and contributed to manuscript writing; X.Z. assisted with SEM ex-

periments; All authors reviewed and revised the manuscript; G.Z. supervised the project.

Corresponding author

Correspondence to [Guofeng Zhang](#).

Competing Interests

The authors declare no competing interests.